ATLAS-LARG-NO-4
December 17, 1994

The Accordion in the end-cap: geometry and characteristics

A. Chekhtman, D. Fouchez, E. Monnier

Centre de Physique des Particules de Marseille, CPPM
IN2P3 et Université d'Aix Marseille II, Marseille, France

Abstract

The purpose of the present note is to described the various constraints used in the definition of the geometry of the end cap electromagnetic calorimeter for ATLAS. Then the chosen geometrical structure is defined and the required working conditions are given. The behaviour of the detector is analysed with these geometrical parameters and some important characteristics such as electronic noise, high voltage current and dynamic range are calculated.

1 Introduction

On the basis of general ideas developped and tested in the framework of the RD3 collaboration [1, 2], the present note describes the adaptation of accordion type calorimeter in the end-cap region. The first part is devoted to the specifications and constraints used to define the geometrical structure of the end-cap electromagnetic calorimeter. In a second part, this structure is presented and all its parameters are discussed. Then various linked information such as cell capacitance, high voltage current, electronic noise and dynamic range is extracted. The parameters obtained in this note should not be considered as frozen and could still be a subject of certain changes.

2 Geometry of the end-cap

2.1 Input parameters

The goal of the calculations presented in this note is to optimize the geometrical structure of the end-cap electromagnetic calorimeter in order to get the best energy resolution and response uniformity in a region of performance optimization.

The boundaries of this region as well as the overall dimensions and position inside the ATLAS detector of the electromagnetic end-caps are considered as defined by the general layout of ATLAS. Namely, the pseudorapidity coverage of the electromagnetic end-caps is considered to be $1.4 < \eta < 3.2$, and the performance optimization is required for at least $1.6 < \eta < 2.8$.

The total calorimeter depth, in terms of radiation lengths, has to be of the order of 28 X_o or more to contain 2 TeV electromagnetic showers without visible deterioration of energy resolution from backward leakage [3].

For technical reasons that are explained in section 2.3 and 2.5, the required rapidity coverage can not be acheived in one accordion structure. Thus, the endcap structure consists of 2 wheels with different numbers and shapes of absorbers.

Monte-carlo studies performed first for the barrel then extended to the endcap structure have shown the need for a number of absorbers close to 360 for the inner wheel [2]. Moreover, the number of absorbers in each wheel has to follow the constraint, from the read-out scheme, of 2^n readout cells in ϕ direction. Then, the average cell size need to be close to the transversal shower dimension. These requirements define the choice of cell granularity $\Delta\eta \times \Delta\phi = 0.025 \times 0.025$ for outer wheel (the same as in the barrel calorimeter) and $\Delta\eta \times \Delta\phi = 0.05 \times 0.05$ for inner wheel. This gives 128 cells for the inner wheel and 256 cells for the outer wheel with 3 absorbers per cell, or 384 (768) absorbers in the inner (outer) wheel.

From mechanical constaints on the cryostat and on the hadron calorimeter dimensions given in [4], the total thickness of active part (with charge collection) of the calorimeter is 51 cm and the distance in the Z direction from the interaction point to the beginning of active part is 362.3 cm. The outer radius is defined by the general layout of ATLAS to be equal to 203 cm.

2.2 The approach to the end-cap accordion geometry optimization

In order to define the endcap geometry, the position of the boundary between small and large wheels has to be choosen as well as, for each wheel, the number of waves, and the radius behaviour of the openning angle and of the lead thickness. These parameters should provide the best signal uniformity in both ϕ and η directions and should satisfy certain technological limitations which will be discussed later on. A better understanding of the optimization procedure can be given by first considering the "ideal" geometry.

Figure 1: *Lay-out of accordion absorbers with "ideal" geometry*

L	total thickness of active part of the calorimeter in Z direction
M	number of waves in Z direction
N	number of absorbers
$\alpha(R)$	openning angle
e(R)	lead thickness
$p = 2\pi R/N$	distance between neighbouring absorbers in ϕ direction
$d = L/2M$	half of zig-zag step
$h = d/tg\frac{\alpha}{2}$	zig-zag height
$l_{zig}(R) = d/sin\frac{\alpha}{2}$	zig-zag length

Table 1: *Geometrical parameters of the "ideal" geometry*

This geometry, shown on the figure 1, uses sharp angles and no materials other than lead or liquid argon. Some of its main parameters, defined in the figure 1, are given in table 1. The amount of lead crossed by a particle does not depend on ϕ if the absorbers are aligned as shown on this picture. This gives an ideal uniformity in the ϕ direction. But the following condition has to be satisfied:

$$h = \beta p, \tag{1}$$

where β is an integer number (in our case $\beta = 3$). The substitution of the defined parameters leads to the following equation:

$$tg\frac{\alpha(R)}{2} = \frac{1}{\beta} \cdot \frac{N}{2\pi R} \cdot \frac{L}{2M}, \tag{2}$$

which gives an expression for $\alpha(R)$:

$$\alpha(R) = 2arctg(\frac{1}{\beta} \cdot \frac{N}{2\pi R} \cdot \frac{L}{2M}). \tag{3}$$

The uniformity in the η direction has to be considered by taking into account that a signal

in such a calorimeter depends not only on the total ionisation in liquid argon (propotional to the energy deposited in LAr), but also on the electric gap and on the high voltage applied. This behaviour is given by:

$$signal \propto (\frac{X_{LAr}}{X_{tot}}) \cdot \frac{v(E) \cdot E}{U}, \tag{4}$$

where U is the high voltage, $E = U/gap$ is the electric field, $v(E)$ is the drift velocity (which could be parametrized as $v(E) \propto E^b$, $b = 0.3$), and (X_{LAr}/X_{tot}) is the sampling fraction. After the substitution of these parameters in the expression, we get:

$$signal \propto (\frac{X_{LAr}}{X_{tot}}) \cdot \frac{U^b}{gap^{b+1}}. \tag{5}$$

Thus, beside the gap, which is a function of the radius in the endcap accordion approach, two independant parameters can control the signal nonuniformity. The lead thickness acts on the energy deposition in LAr. The high voltage acts on the signal produced by the deposited charge in LAr. Therefore, a variable high voltage can be applied to compensate for the gap variations and get a constant signal. In this case, sampling fraction nonuniformities could also be compensated if the high voltage is calculated by the following formulae:

$$U \propto (\frac{X_{tot}}{X_{LAr}})^{\frac{1}{b}} \cdot gap^{\frac{1}{b}+1}. \tag{6}$$

The sampling fraction should be rather uniform to provide an energy resolution independent of η. This is the reason why the deposited energy and the produced signal are tried to be kept uniform in the present calculation. An expression of the sampling fraction can be given by considering a thin cylindrical layer of a calorimeter with a radius R and a thickness ΔR. The volume of lead in such a layer could be expressed by:

$$V_{Pb} = e(R) \cdot l_{zig}(R) \cdot \Delta R \cdot 2MN, \tag{7}$$

which gives after a division by the layer cross section ($\Delta S = 2\pi R \Delta R$), the equivalent thickness of lead:

$$L_{Pb} = \frac{e(R) \cdot l_{zig}(R) \cdot 2M}{\frac{2\pi R}{N}}. \tag{8}$$

In the considered case of only two materials (lead and liquid argon), the inversed sampling fraction (X_{tot}/X_{LAr}) could be derived from L_{Pb} as follows:

$$(\frac{X_{tot}}{X_{LAr}}) = 1 + \frac{X^0_{LAr}}{X^0_{Pb}} \cdot \frac{1}{\frac{L_{tot}}{L_{Pb}} - 1}, \tag{9}$$

where, X^0_{LAr} and X^0_{Pb} are the radiation length respectively for LAr and for lead, and $L_{tot} = d \cdot 2M$ is the total thickness of the calorimeter. Thus the condition $(X_{tot}/X_{LAr}) = const$ is equivalent to $L_{Pb}/L_{tot} = const$ which leads, from equation 8, to:

$$\frac{e(R) \cdot l_{zig}(R)}{d \cdot \frac{2\pi R}{N}} = const. \tag{10}$$

Therefore, the lead thickness as a function of the radius can be express by:

$$e(R) \propto \frac{2\pi R}{N} \cdot \frac{d}{l_{zig}(R)}, \tag{11}$$

which turned out to be, after sustitution of $l_{zig}(R)$:

$$e(R) \propto \frac{2\pi R}{N} \cdot sin\frac{\alpha(R)}{2}. \tag{12}$$

Thus, the sequence of endcap parameters calculation is the following:

1. determine $\alpha(R)$ using (3)
2. determine e(R) from (12)
3. determine U(R) from (6)

2.3 Boundary position between two wheels

The simple relation, $tg\frac{\alpha}{2} \propto \frac{1}{R}$, derived from the condition 3, shows that giving α_{in} and α_{out}, the values of the boundary openning angles, leads to give the inner R_{in} to outer R_{out} radius ratio of one wheel of endcap accordion. This can be expressed by:

$$\frac{tg\frac{\alpha_{in}}{2}}{tg\frac{\alpha_{out}}{2}} = \frac{R_{out}}{R_{in}}. \tag{13}$$

Limitations in the technologies used in the production of absorbers of accordion shape imply that the openning angle α should be kept in the following boundaries:

$$60^0 < \alpha < 120^0. \tag{14}$$

These boudaries and equation 13 give a constraint on the outer to inner radius ratio for one wheel of endcap:

$$\frac{R_{out}}{R_{in}} < 3. \tag{15}$$

But, according to the overal dimensions of endcap calorimeter, defined in section 2.1, the outer to inner radius ratio for the whole endcap is 6.7. Thus, in order to be close to the above constraint, it has been chosen to have a two wheels geometry for the endcap calorimeter.

An almost identical R_{out}/R_{in} ratio for both wheels should be taken to ease the building of the wheels. But such a choice would mean a crack position between the two wheels in the middle of the η coverage region $1.4 < \eta < 3.2$, i.e. $\eta_{crack} = 2.3$. And this leads to a width of the kapton electrodes for the inner wheel larger than 61 cm which is difficult to produced with standard technologies available today. Thus, $\eta_{crack} = 2.4$ has been chosen as a good compromise. In this case, $R_{out}/R_{in} = 3.00$ for the outer wheel and $R_{out}/R_{in} = 2.55$ for the inner wheel, which is not symmetrical, but still in the range.

2.4 Different factors affecting the uniformity of response

In the section 2.2 we have got an expression of the openning angle and of the lead thickness that provide the signal uniformity for an "ideal" endcap calorimeter. These formulae should be modified to be closer to the reality. The presence of inactive materials others than lead (stainless steel, glue,kapton) with a thickness independent of the radius have to be taken into account. Thus, the optimal lead thickness given by equation 12 should be slightly modified. Moreover, the angles of accordion are not sharp, they have a curvature radius. Then, the condition for the absorbers alignement should be modified as well.

2.4.1 The effect of inactive materials

By analogy with the expression 8, the equivalent total thickness in the calorimeter for a material i is:

$$L_i = \frac{e_i \cdot l_{zig}(R) \cdot 2M}{2\pi R/N}, \tag{16}$$

where e_i is the thickness of a layer of material i per one absorber plate. Then, the equivalent thickness of liquid argon can be expressed by:

$$L_{LAr} = L_{tot} - (e_{Pb}(R) + \sum_i e_i) \cdot l_{zig}(R) \cdot \frac{N}{2\pi R} \cdot 2M, \tag{17}$$

where $e_{Pb}(R)$ is the thickness of lead. The number of radiation length in liquid argon X_{LAr} is equal to :

$$X_{LAr} = L_{LAr}/X^0_{LAr} = \frac{2M}{X^0_{LAr}}(d - (e_{Pb}(R) + \sum_i e_i) \cdot l_{zig}(R) \cdot \frac{N}{2\pi R}). \tag{18}$$

Thus, the total number of radiation lengths in the inactive materials X_{abs} can be defined as:

$$X_{abs} = X_{tot} - X_{LAr} = (\frac{e_{Pb}(R)}{X^0_{Pb}} + \sum_i \frac{e_i}{X^0_i}) \cdot l_{zig}(R) \cdot \frac{N}{2\pi R} \cdot 2M. \tag{19}$$

From the evident equation:

$$\frac{X_{abs}}{X_{LAr}} = \frac{X_{tot}}{X_{LAr}} - 1, \tag{20}$$

the condition of the sampling fraction uniformity can be expressed in the following form:

$$\frac{X_{abs}}{X_{LAr}} = const = \xi. \tag{21}$$

Then, after substitution of (18) and (19), this condition becomes:

$$(d - (e_{Pb}(R) + \sum_i e_i) \cdot l_{zig}(R) \cdot \frac{N}{2\pi R}) \cdot \frac{\xi}{X^0_{LAr}} = (\frac{e_{Pb}(R)}{X^0_{Pb}} + \sum_i \frac{e_i}{X^0_i}) \cdot l_{zig}(R) \cdot \frac{N}{2\pi R}. \tag{22}$$

Solving the previous equation leads to the following expression for the lead thickness:

$$e_{Pb}(R) = [\frac{2\pi R}{N} \cdot \frac{d}{l_{zig}(R)} \cdot - \sum_i e_i(\frac{X^0_{LAr}}{X^0_i} + \xi)]/(\frac{X^0_{LAr}}{X^0_{Pb}} + \xi), \tag{23}$$

which is naturally compatible with (11), when $e_i = 0$.

2.4.2 The effect of round folds of accordion

The presence of non-zero curvature radius in a fold region alters the uniformity in ϕ direction. Thus a modification of the alignement condition is necessary. The alignement principle illustrated by figure 2 can be used to minimize the nonuniformities produced by round folds.

In fact, the alignement condition 1 is unchanged, but the value of accordion height h is defined now, as shown on figure 2, as a distance between the extreme points of accordion, and can be expressed by:

$$h = \frac{d}{tg\frac{\alpha}{2}} - \frac{2\rho}{sin\frac{\alpha}{2}} + 2\rho + e, \tag{24}$$

Figure 2: *Lay-out of accordion absorbers with round angles.*

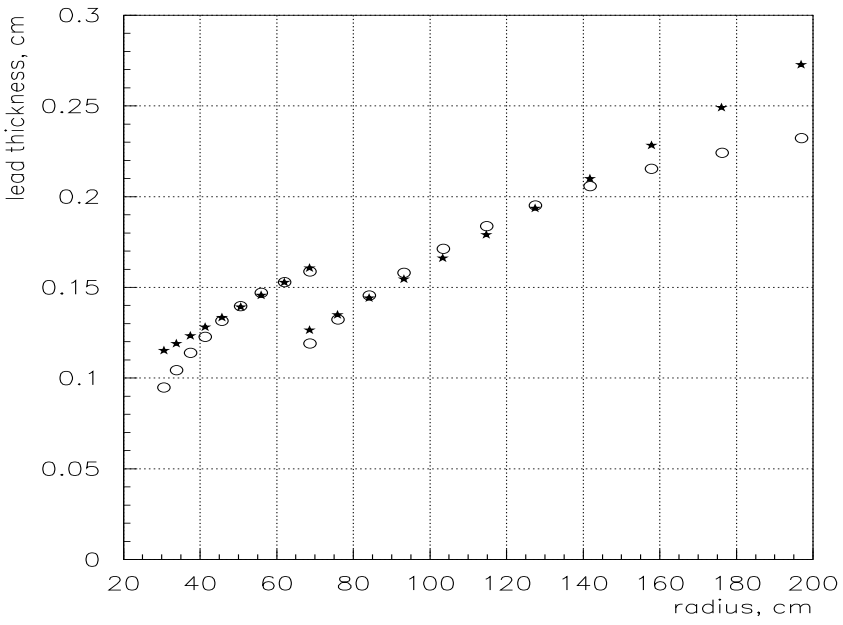

Figure 3: *Lead thickness as a function of radius; (a) circles - optimal geometry, (b) stars - linear approximation.*

where ρ is the curvature radius corresponding to the center of absorber plate and e is the total thickness of the absorber. The formulae 23 for the lead thickness is correct in the case of round folds, but the expression for l_{zig} used in an ideal case, should be replaced by:

$$l_{zig} = \frac{d}{sin\frac{\alpha}{2}} - \frac{2\rho}{tg\frac{\alpha}{2}} + (\pi - \alpha)\rho. \tag{25}$$

After these modifications, equations 1 and 23 become nonlinear, but they can be solved numerically by iterative method in order to obtain $\alpha(R)$ and $e_{Pb}(R)$. This solution is called "the optimal geometry".

The behaviour of $e(R)$ and l_{zig} as a function of the radius, got from such calculations, are shown on figure 3 and 4 for the whole range of radius, covering both wheels. These behaviours are significantly nonlinear inside each wheel. Such a shape cannot be done with the nowadays technologies used in the absorbers production. Therefore, only a linear behaviour can be achieved and a linear approximation for each wheel has then been chosen as shown on the figures 3 and 4. The average deviation from the optimal curve has been minimized in the region of performance optimization defined in section 2.1. Starting from the linear approximation of $l_{zig}(R)$, the equation 25 can be solved to determine $\alpha(R)$ and then $e_{Pb}(R)$ from equation 23. This solution is called "the approximative geometry". In this last case the condition 1 is not satisfied. Thus, parameter $\Delta h = h - \beta \cdot 2\pi R/N$, characteristic of the defect of alignement can be defined.

2.5 Number of waves

On the figure 5 the behaviour of the accordion openning angle as a function of η is shown for different number of waves M in the inner and the outer wheels. $M = 9$ for the outer wheel and $M = 12$ for the inner wheel are the compromise values chosen to satisfy the technological limitation given in expression 14 on the openning angle.

2.6 Analytical calculations of the geometrical parameters

The behaviour of the different parameters as a function of η are presented on the figures 6 to 14 for two cases: optimal geometry (circles) and approximate geometry(stars). In the optimal case, a constant sampling fraction $X_{LAr}/X_{tot} = 0.075$ was chosen to provide a total calorimeter thickness larger than 28 radiation lengths. In the approximate geometry case, a deviation of the sampling fraction (fig.10) from a constant value is seen. It is compensated by a high voltage variation (fig.14).

The analitical calculations presented here are planned to be completed by detailed Monte-Carlo simulation of a shower development in the end-cap. From those studies the energy resolution and ϕ-modulation of a signal will be obtained.

In the calculation of the high voltage, a minimum value of 0.3 kV/cm for the electric field has been taken in order to have always normal charge collection conditions. This value was the one used in the tested prototype [1] [5]. It is taken for the inner radius of each wheel as a limit. Then the other high voltage values are calculated from equation 6 to get a constant current signal inside each wheel. To get an identical signal for both wheels the amplifiers for outer wheel will have 10% higher gain than for inner wheel.

To compensate the decrease of the sampling fraction for approximate geometry at $\eta < 1.6$ (see fig.10), the amplifiers in this region have a gain 25% higher than in inner wheel. This permits to keep the high voltage less than 3 kV for this part of the calorimeter.

In these calculations the high voltage was considered to be a function of radius, which is not the case for the real calorimeter. High voltage in reality is fixed for read-out cells, having a

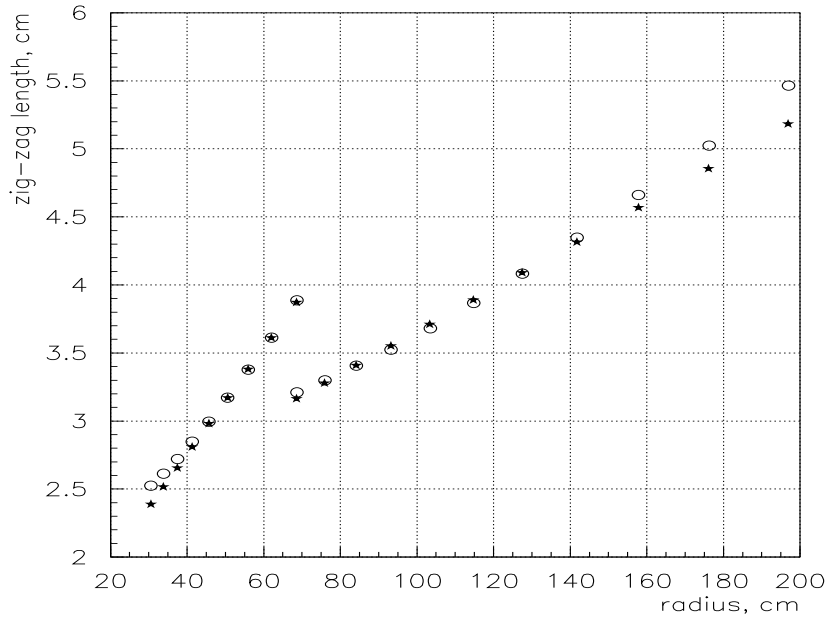

Figure 4: *Zig-zag length as a function of radius; (a) circles - optimal geometry, (b) stars - linear approximation.*

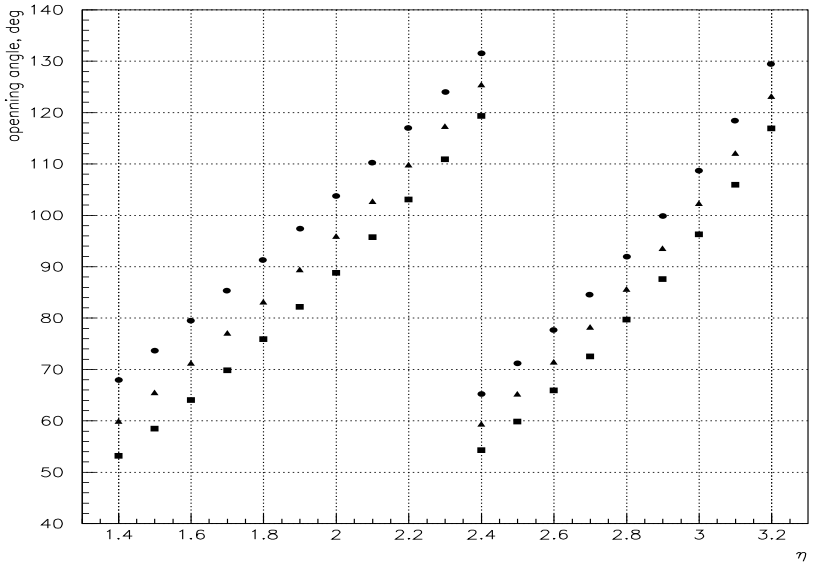

Figure 5: *Openning angle versus η for accordion shape absorbers with different number of waves (M). Outer wheel ($\eta < 2.4$): circles - M=8, triangles - M=9, squares - M=10; inner wheel ($\eta > 2.4$): circles - M=11, triangles - M=12, squares - M=13.*

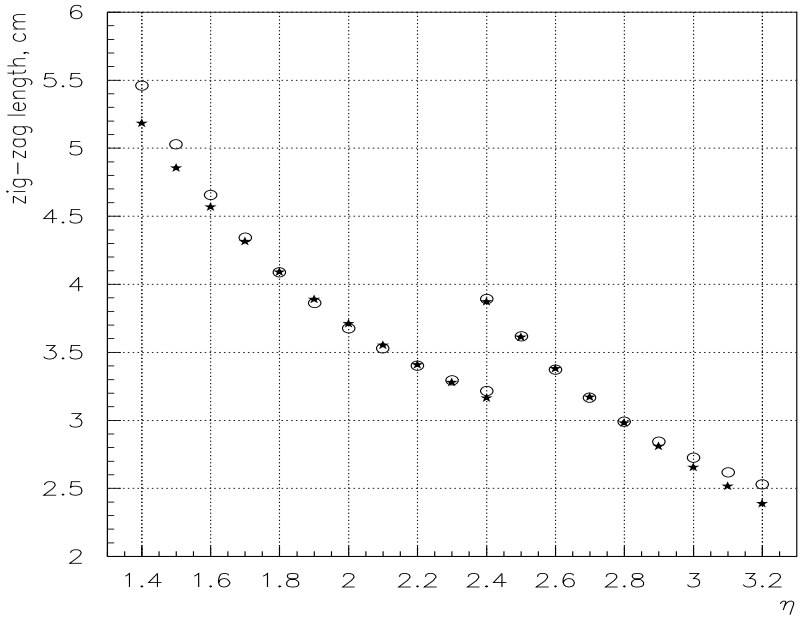

Figure 6: *Zig-zag length as a function of η; (a) circles - optimal geometry, (b) stars - approximate geometry.*

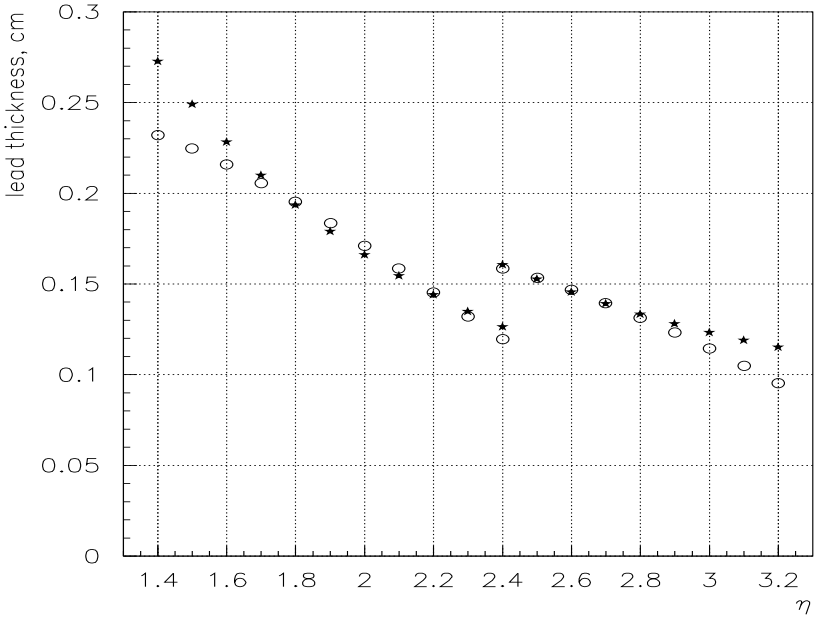

Figure 7: *Lead thickness as a function of η ; (a) circles - optimal geometry, (b) stars - approximate geometry.*

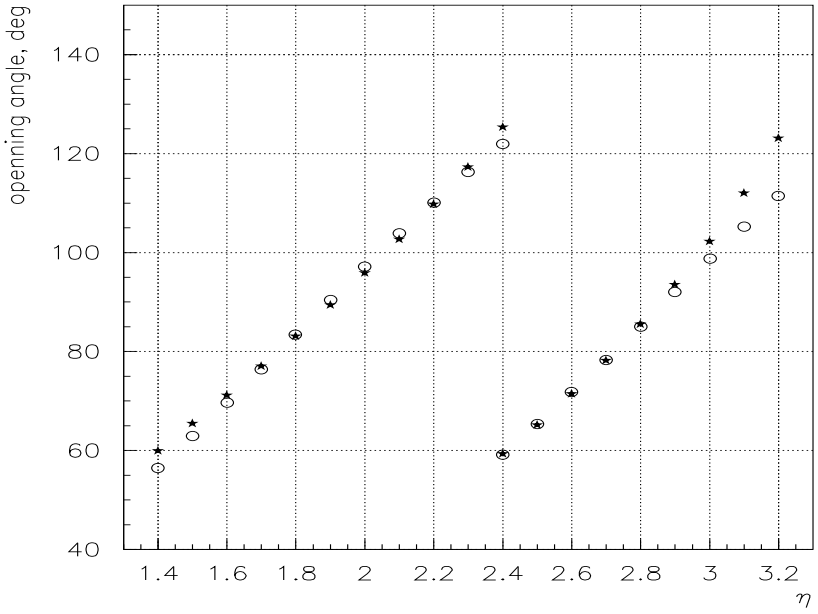

Figure 8: *Openning angle as a function of η ; (a) circles - optimal geometry, (b) stars - approximate geometry.*

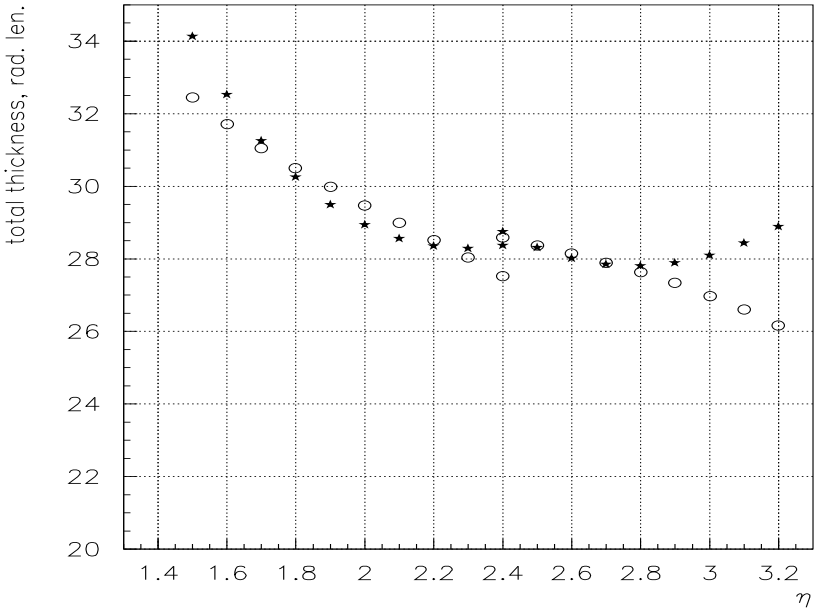

Figure 9: *Total number of radiation lengths as a function of η ; (a) circles - optimal geometry, (b) stars - approximate geometry.*

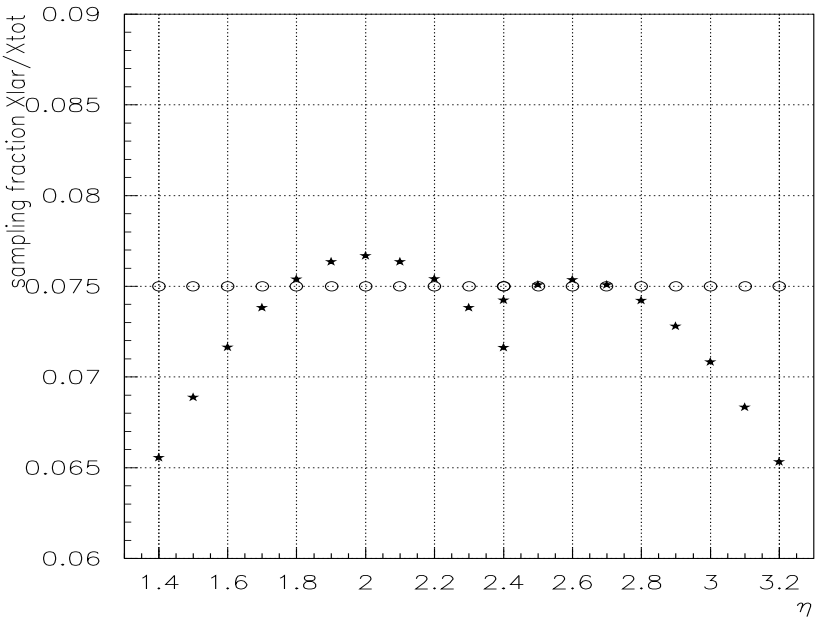

Figure 10: *Sampling fraction X_{LAr}/X_{tot} as a function of η ; (a) circles - optimal geometry, (b) stars - approximate geometry.*

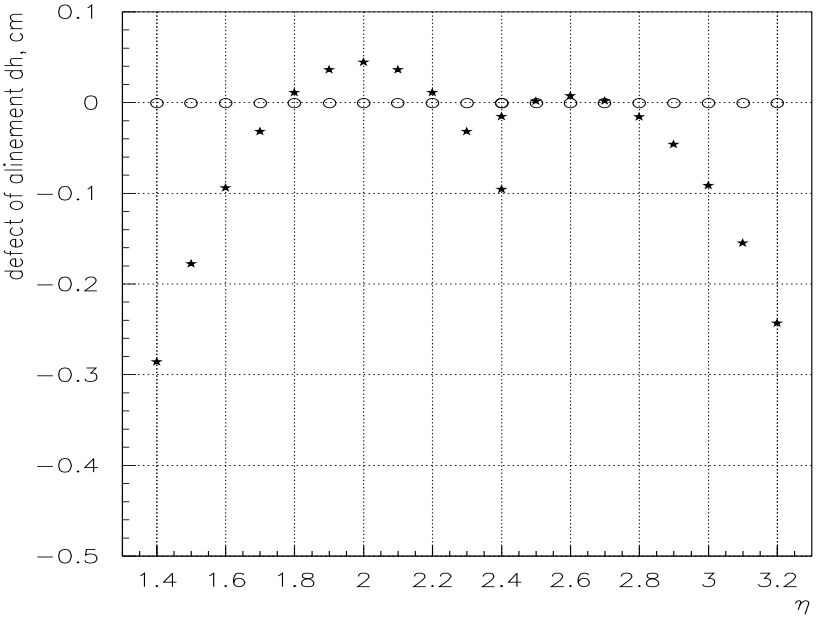

Figure 11: *Defect of alinement Δh as a function of η ; (a) circles - optimal geometry, (b) stars - approximate geometry.*

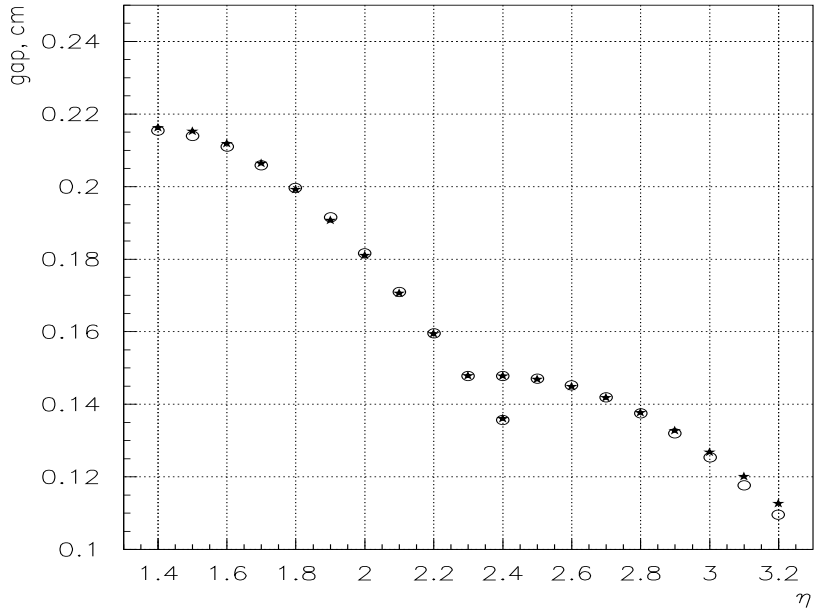

Figure 12: *Electric gap as a function of η ; (a) circles - optimal geometry, (b) stars - approximate geometry.*

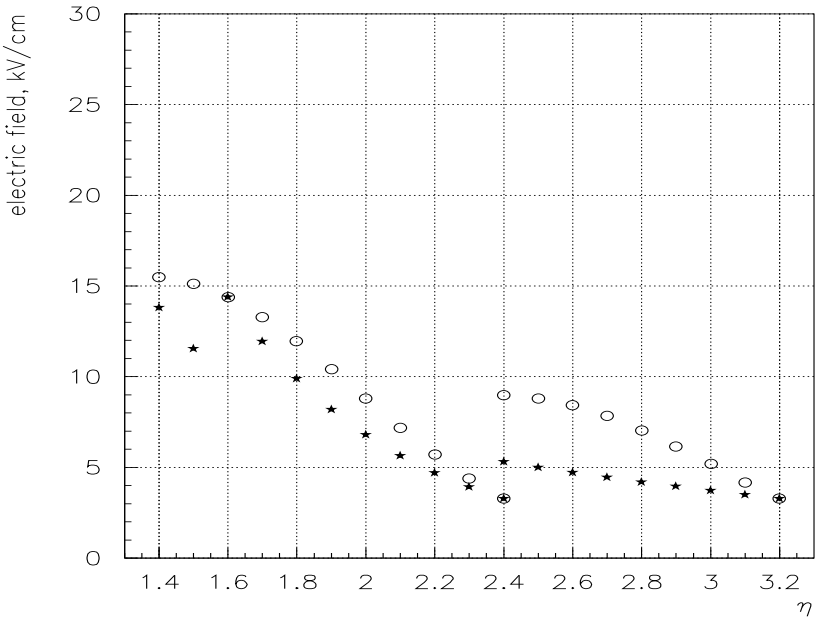

Figure 13: *Electric field as a function of η ; (a) circles - optimal geometry, (b) stars - approximate geometry.*

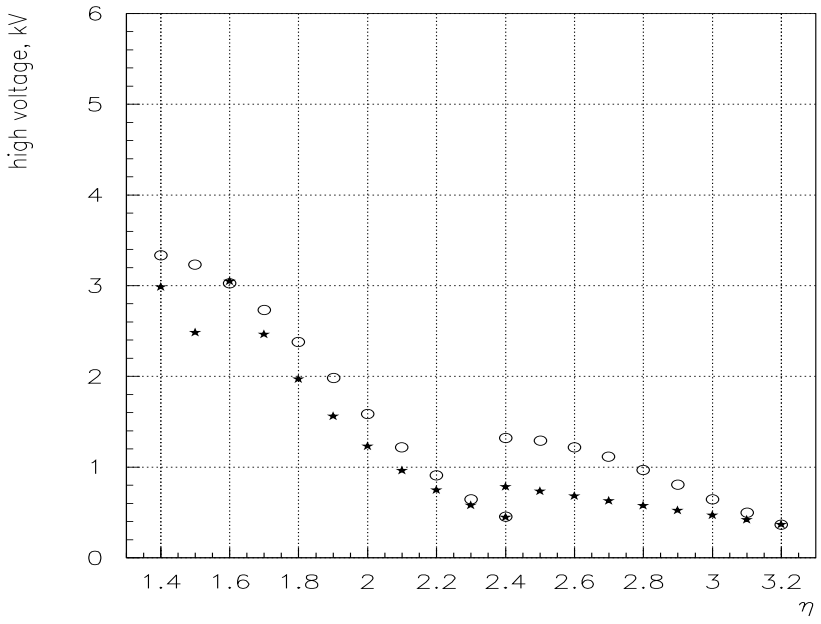

Figure 14: *High voltage as a function of η ; (a) circles - optimal geometry, (b) stars - approximate geometry.*

pointing geometry. However, as it was shown by the prototype beam tests [5], the linearity of the calorimeter can be preserved by using different high voltages for longitudinal segmentations of a cell. The appropriate values of high voltages will be chosen from the detailed Monte-Carlo simulation.

3 Induced behaviour of the detector linked to the choosen geometry

3.1 Detector capacitances

The detector capacitances have been calculated for each readout pad on each Kapton foil by using the parameters given in section 2.6. It is not an exact calculation. We used a planar capacitor aproximation with the following formulae:

$$C_d = \epsilon_r \epsilon_0 \times \frac{Surface}{Gap}. \tag{26}$$

$\epsilon_r = 1.6$ is the relative permittivity of liquid argon, $Surface$, is the surface of the pad aproximated by using the exact calculation of its projected surface onto the accordion plane times the ratio of the exact length of a waves to the corresponding projected length. Gap, is the mean gap calculated at the mean starting radius of the pad strip. For information, we have $\epsilon_{Kapton} \simeq 3.5$ and $\epsilon_{epoxy} \simeq 3.5-5$. The strip capacitance due to the argon gap has been calculated and is showed on figure 15. This capacitance is the individual capacitance of each Kapton strip. On each side of a Kapton foil, there is an high voltage strip and a signal strip burried between them inside the Kapton electrode. Due to the small thickness of the Kapton foil compared to the argon gap, the capacitance of this gap is much smaller than the one of Kapton. Thus, because these two capacitance are added in series, the effect of the Kapton capacitance can be neglected. So, the detector capacitance can be aproximated to the two liquid argon gap (HV strips) capacitance added in parallel.

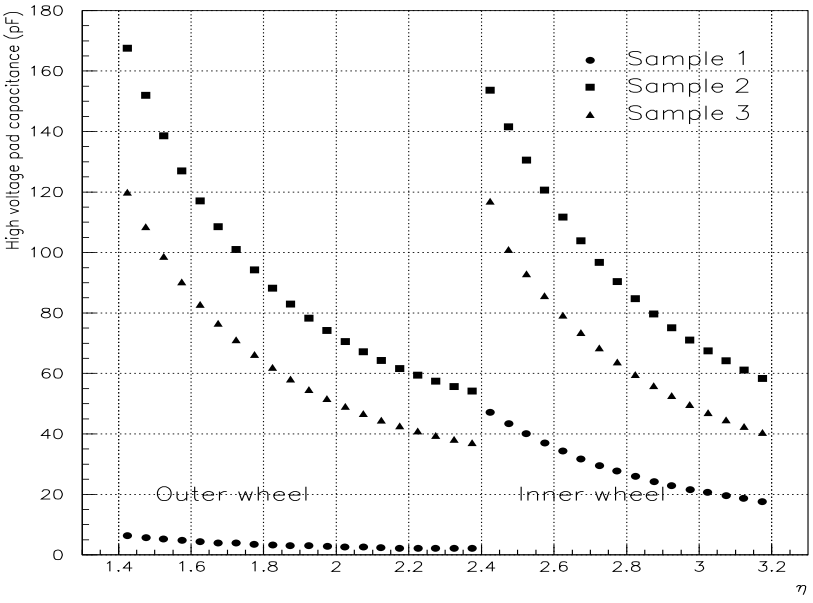

Figure 15: *Endcaps high voltage pad capacitance versus* η

As described in [7], the outer wheel is made of thin strips groupped by 12 in ϕ for the first depth segmentation ($5X_\circ$), of strips groupped by 3 in the second segmentation ($14X_\circ$) and groupped by 6 in the third one ($10X_\circ$). In the inner wheel, the chosen depth segmentation is roughly the same as for the outer wheel ($5X_\circ$, $14X_\circ$, $9X_\circ$) but without thin strips in the first segmentation. Then the strips are groupped in ϕ by 3, 3, and 6 for respectively first, second and third segmentation. With these parameters, the detector capacitance of each signal cell has been calculated and is showed on the figure 16.

3.2 Electronic noise

The signal cell of the end cap calorimeter are read out with $0T$ preamplifiers. This preamplifier and the relation between its electronic noise and the detector capacitance have been described in [6]. Using the behaviour of the equivalent noise charge (ENC) and of the peaking time with respect to the detector capacitance as shown in [6], the electronic noise for each signal cell can be computed.

But, in order to give this result in terms of energy deposited, one need to know the ratio between energy deposited in a cell and induced current. Thus, the charge deposited by an incoming particle in the liquid argon is needed. The total ionisation charge deposited is given by [8]:

$$Q = \frac{E}{W_i}\eta_s a_m \tag{27}$$

in which Q is the value of the deposited charge (Q electrons and Q ions), E is the incoming particle energy, $W_i = 26eV$ is the energy needed to create one pair electron-ion in the liquid argon, η_s is the dE/dx sampling fraction and $a_M = 0.7$ is a supression factor for electromagnetic showers. Usually Q is calculated as a factor for $1MeV$ deposited energy. We will now use this definition for Q. For the encaps, after an exact calculation of the dE/dx sampling fraction, we got roughly a value of (in the calculation the exact value will be used):

$$Q = 5500\ (e^-/MeV\,deposited). \tag{28}$$

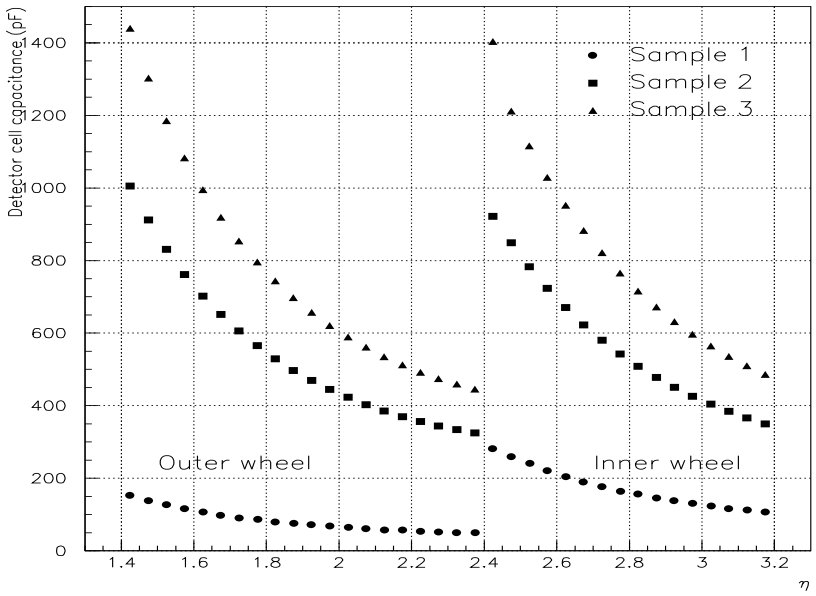

Figure 16: *Endcaps cell capacitance versus η*

Then, the conversion of an electronic noise current into a noise in MeV is given by the conversion factor:

$$I_0 = Q/t_{dr}, \tag{29}$$

where t_{dr} is the drift time for charge deposited in the liquid argon gap. This drift time is linked to the applied electric field as said in section 2.6. Therefore, by using the electric field and the gap calculated in section 2.6, we got the complete behaviour shown on figure 17 for the various signal cells. A simple way of calculating this noise has been given in [6] and use the expression : $\sigma_{el}(MeV) = 19 \bigoplus 0.075 * C_d(pF)$. The corresponding behaviour is shown on figure 18.

3.3 High voltage current

To ease the choice of the type of high voltage needed for the electromagnetic endcaps, two quantities are important to know: the required voltage range given in section 2.6 and the forseen current.

There are two possible high voltage current sources in the endcaps. The first one is produced by high energy electrons produced in the Z' decay. The second one is coming from the constant background of pile up particles seen by each endcap cell.

3.3.1 Current induced by a single particle

In order to calculate the current induced by a single particle for a given high voltage cell, we need to know the deposited charge (as defined in section 3.2) and the integration time at the high voltage level (a few micro seconds). This time is $R_{HT}C_{HT}$ where C_{HT} (figure 15) is the high voltage pad capacitance and $R_{HT} = 1M\Omega$ is the value of the resistor connected to each high voltage pad. The deposited current in one cell is given by the following expression:

$$I_{cell} = \frac{2Qq_{e^-}E(MeV)}{R_{HT}C_{HT}}. \tag{30}$$

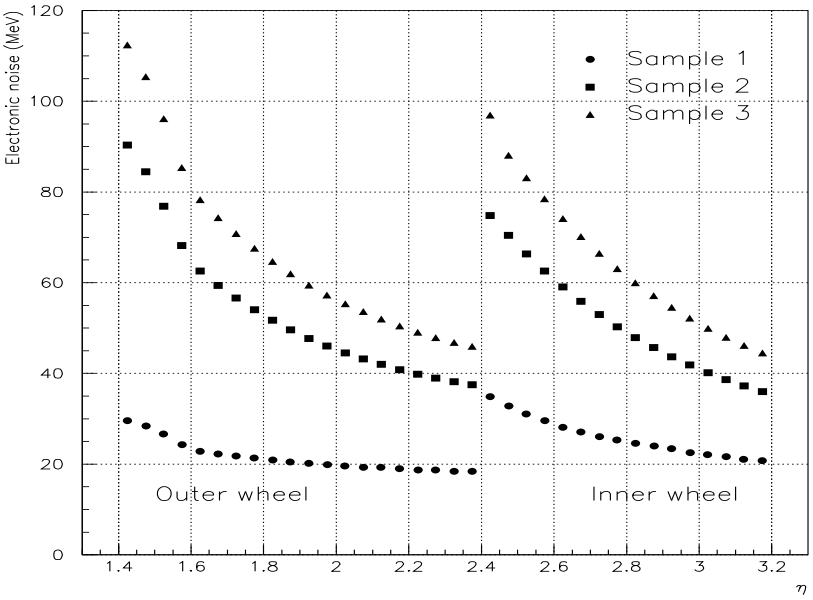

Figure 17: *Electronic noise on each Endcap cell versus* η

One should mention that the RC of a group of identical cell connected in parallel is the same as for an elementary cell (a pad cell (Kapton))(if there are "n" "Kapton cells" in a read out cell, the corresponding "RC" is $nC \times R/n$).

3.3.2 ***Pile-up current***

The mean energy deposited by a standard event in an endcap cell with a 0.05×0.05 granularity has been estimated by Monte-Carlo studies. The results are given in figure 19. Furthermore, at a luminosity of 10^{34}, there is an average of 18 such events per bunch crossing. This leads to the mean energy deposited in a 0.05×0.05 cell represented on figure 20. These calculations have been made without any sampling in depth. But the values are low enough to assume that the energies are mainly deposited in the first sampling ($5X_\circ$).

As defined in the previous section, the high voltage integration time is long enough with respect to the bunch crossing time to allow several bunch crossing ($n_{bunch} = R_{HT}C_{HT}/25 \cdot 10^{-9}s$) to occure in the mean time. Thus, by taking the expression 30 given for a single event times n_{bunch}, the induced current becomes:

$$I_{cell} = \frac{2Qq_{e^-} < E_{cellpileup}(MeV) >}{25 \cdot 10^{-9}}, \tag{31}$$

which leads, taking the rough value of $Q = 5500$, to the following expression (independant of the cell capacitance and of the cell resistance) :

$$I_{cell} = (70nA) < E_{cellpileup}(MeV) > . \tag{32}$$

But each high voltage power supply is forseen [7] to be connected to $16(\phi(0.05)) \times 1(\eta(0.05))$ cells for the inner wheel and $4(\phi(0.2)) \times 16(\eta(0.003125))$ strip cells for the outer wheel. This gives a high voltage granularity of $0.8(\phi) \times 0.05(\eta)$. Then the total current on each high voltage is given

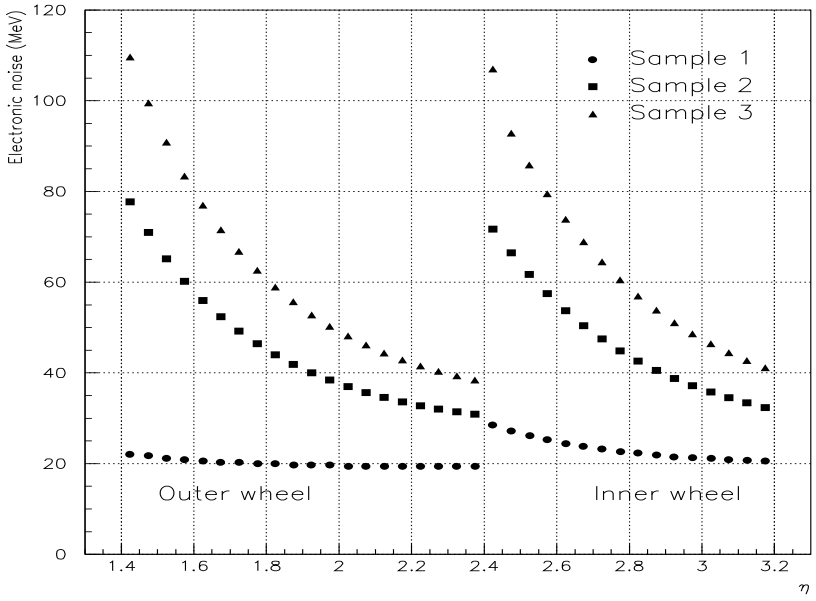

Figure 18: *Electronic noise on each Endcap cell versus η calculated with $\sigma_{el} = 19 \bigoplus 0.075 * C_d$ (pF) in MeV*

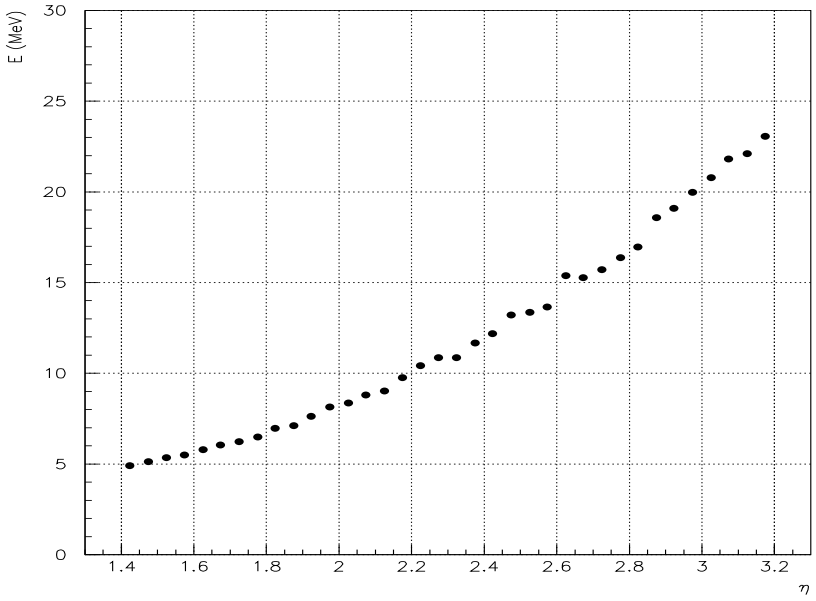

Figure 19: *Mean energy deposited by standard events in a 0.05×0.05 endcap cell versus η*

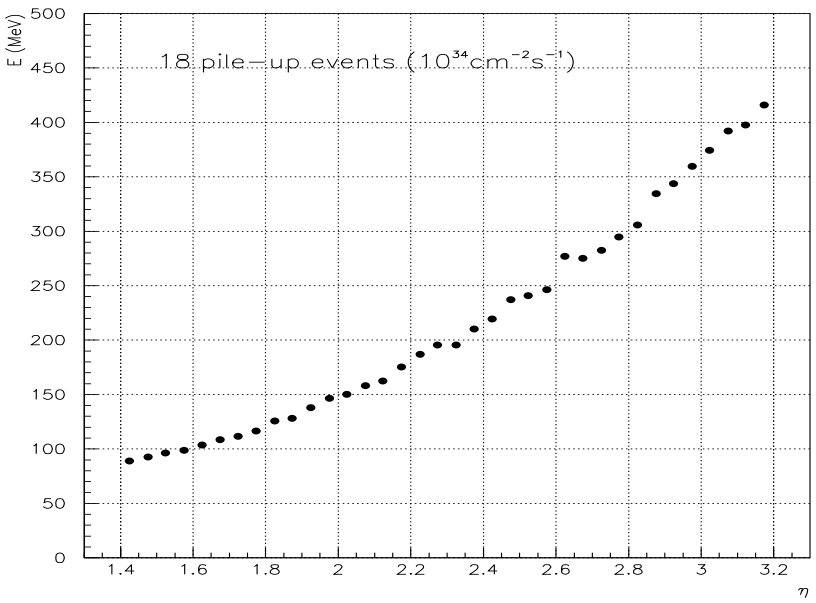

Figure 20: *Mean pile-up energy deposited in a* 0.05×0.05 *endcap cell versus* η

by (with $Q = 5500$) :

$$I_{HV\,cell} = (1.1\mu A) < E_{0.05\times 0.05 cellpileup}(MeV) >, \tag{33}$$

which leads, by using the results given in figure 20 and the exact calculation of Q to the current given in the figure 21. It has been assumed, in first approximation, that the total deposited energy in each high voltage cell could be estimated by using a calculation made for 0.05×0.05 cells.

The induced high voltage loss has to be calculated at the level of each "high voltage pad resistor". In the inner wheel, one cell is based on three Kapton foils, and each Kapton foil is double sided. Thus, as the "pad resistor" is a $1M\Omega$ resistor, the induced loss is given for an average $Q = 5500$ by :

$$HV_{loss} = 1M\Omega \times \frac{(70nA)}{6} < E_{0.05\times 0.05 cellpileup}(MeV) >, \tag{34}$$

which leads to a range of 2.5 to 4.5V of induced high voltage loss (cf fig. 22). In the outer wheel, the energy deposited in a region of 0.05×0.05 granularity is distributed on to six double sided Kapton foils with 16 η strips on each. Thus, if the "pad resistor" is still a $1M\Omega$ resitor, the induced loss is given by :

$$HV_{loss} = 1M\Omega \times \frac{(70nA)}{96} < E_{0.05\times 0.05 cellpileup}(MeV) >, \tag{35}$$

which leads to a range of 0.06V to 0.16V of induced high voltage loss (cf fig. 23). As a matter of fact, the high voltage current for each high voltage pad strip is just the high voltage loss divided by $1M\Omega$ and is represented on figure 22 and 23 on the left scale.

3.3.3 High energy electrons current

The mean energy deposited in the EndCaps by electrons created in the decay of a 5 TeV Z' have been estimated by using Monte-Carlo simulations. The η distribution and the momentum

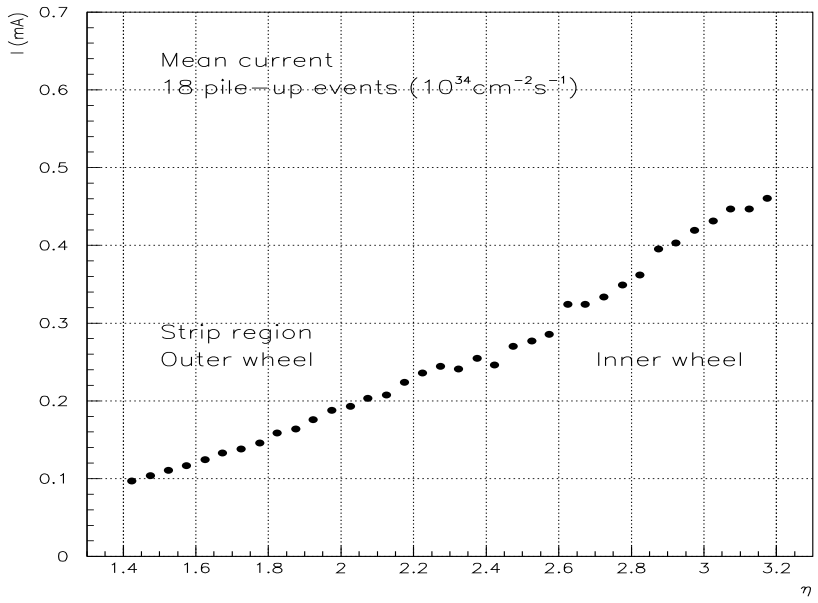

Figure 21: *Pile-up current on the EndCaps high voltage power supply versus* η

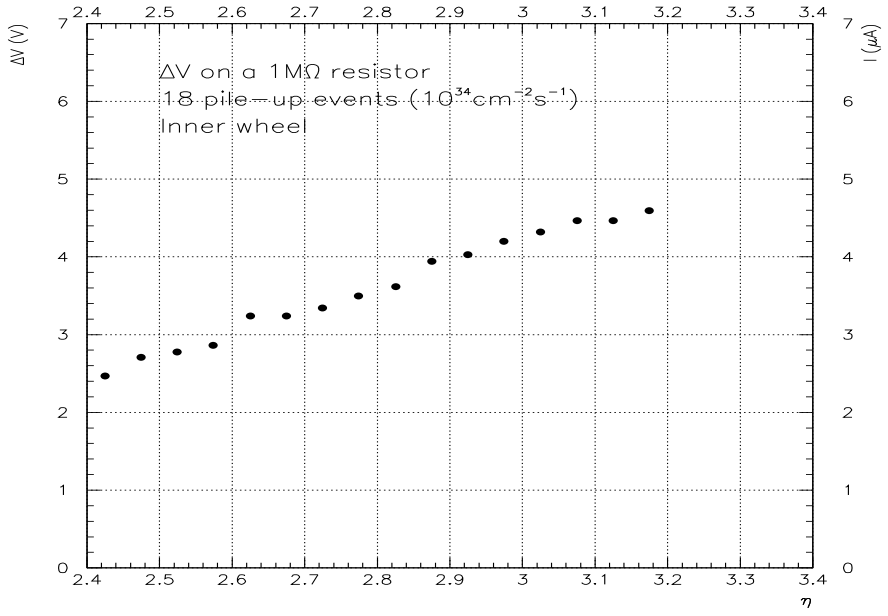

Figure 22: *High voltage loss induced on each cell by the pileup versus* η *for the inner wheel of the EndCaps* ($1M\Omega$ *resistor). Right scale: induced current*

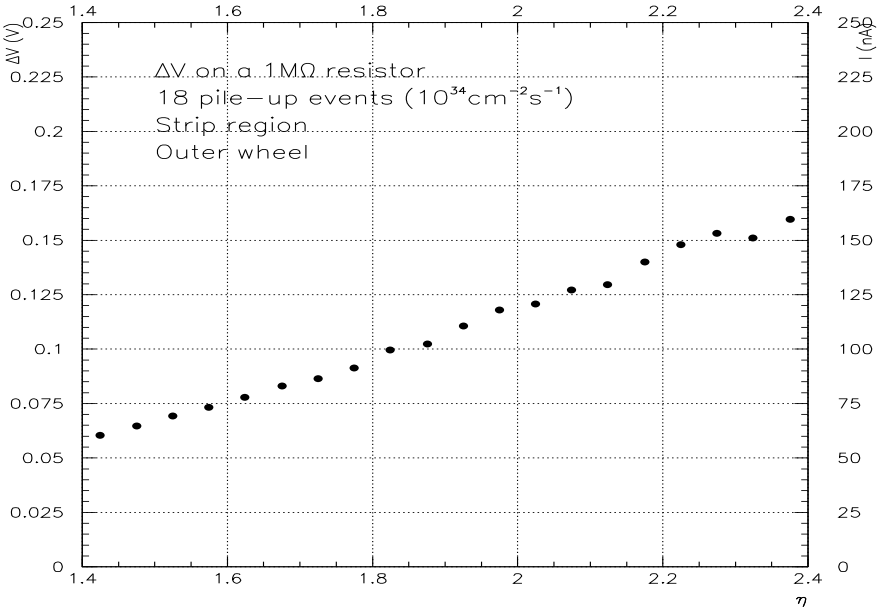

Figure 23: *High voltage loss induced on each strip by the pileup versus η for the outer wheel of the EndCaps ($1M\Omega$ resistor). Right scale: induced current*

distribution of such electrons are given in figure 24. One can assume, regarding the very small cross section of such events, that only one such event can be produced at least in the integration time given in section 3.3.1. In addition, the energy is high enough to assume that the full energy can be seen, in first approximation by a "HV cell" in the inner wheel. Thus the maximum induced current is given by :

$$I_{cell} = \frac{2Qq_{e^-}E(MeV)}{R_{HT}C_{HT}}, \tag{36}$$

which leads to (assuming a typical mean capacitance of 30pF and a $1M\Omega$ resistance :

$$I_{cell} = 60\mu A E_{e^-}(TeV), \tag{37}$$

This means that, according to the figure 24, the current on an high voltage of the inner wheel is below $300\mu A$. For the outer wheel the currents in the various sectors will also be below this value.

3.4 Maximum signal in the endcap

The maximum signal that can be seen by the endcap calorimeter is the one induced by the decay of a 5 TeV Z'. Assuming that we want to see 95% of these high energy events, this means, according to figure 24 that the detector has to withstand e^- with a momentum of 5 TeV. The longitudinal energy profile given in the PDG [9] rescaled at a 5 TeV energy allow for a first estimation of the maximum signal deposited by an electron of 5 TeV in the inner wheel and in the outer wheel. One can take as for the barrel calorimeter an average of 60% of the energy deposited in the central cell. Taking an average of $2X_\circ$ of matters before the active region (28 $X_\circ$) of the calorimeter and assuming that in the worse case, the electron has started its shower at the beginning of this forward matters leads to the energy given in table 2.

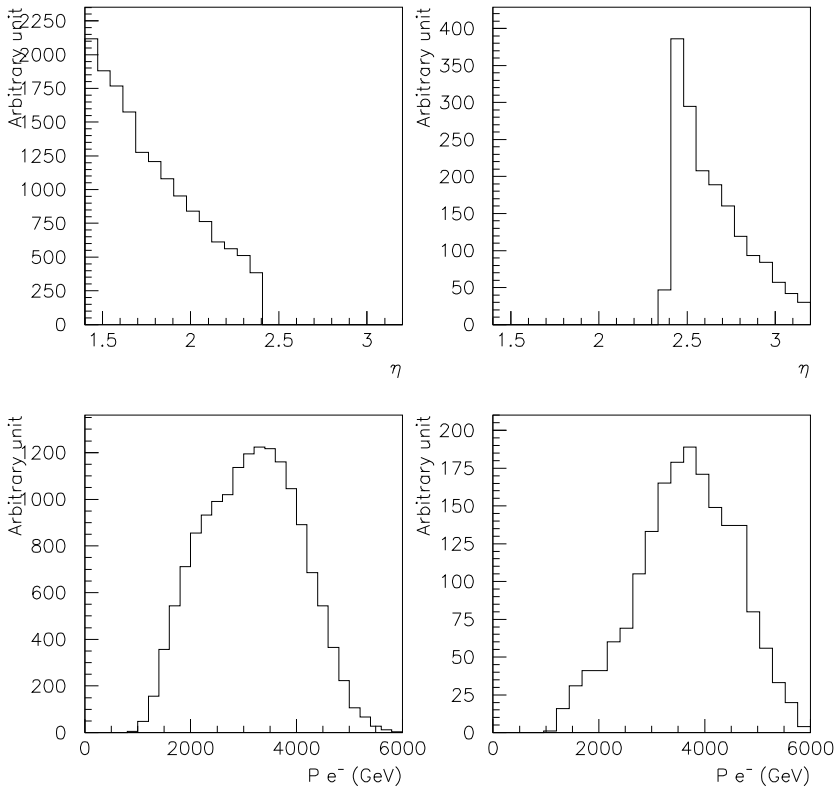

Figure 24: *η and momentum distribution of electrons produced in the Z' decay in the inner and the outer wheels*

outer	Front	Middle	Back
Depth	5	14	10
Maximum energy	200 GeV	2500 GeV	500 GeV
Inner	Front	Middle	Back
Depth	5	14	9
Maximum energy	200 GeV	2500 GeV	500 GeV

Table 2: Maximum signal in each endcap wheels

References

[1] RD3 Status Report. CERN/DRDC 93-4
[2] RD3 Status Report. CERN/DRDC 94-18
[3] K.Jacobs,A.Kiryunin, ATLAS internal note CAL-NO-20 (1993)
[4] P.Dargent, J.-L. Gimenez, L.Martin. ATLAS internal note LARG-NO-6 (1994)
[5] A.Chekhtman et al. ATLAS internal note CAL-NO-67 (1994)
[6] C. de La Taille et al., NIM A343 (1994) 598-605
[7] P. Fassnacht, E. Monnier, S. Tisserant, ATLAS internal note LARG-NO-7 (1994)
[8] C. de La Taille, Electronic noise in Lar calorimetry RD3 internal note 45 (1993)
[9] Particle Data Group, Review of Particle Properties, Phys. Rev. D, Vol 50, N0 3